Supporting Information

PtTe Monolayer: Two-dimensional Electrocatalyst with High Basal Plane Activity towards Oxygen Reduction Reaction

Yu Wang,[†] Yafei Li,[*,†] and Thomas Heine[*,‡,§]

[†]Jiangsu Collaborative Innovation Centre of Biomedical Functional Materials, Jiangsu Key Laboratory of New Power Batteries, School of Chemistry and Materials Science, Nanjing Normal University, Nanjing 210023, China.

[‡]TU Dresden, School of Science, Theoretical Chemistry, Bergstraße 66c, 01062 Dresden, Germany.

[§]Helmholtz-Zentrum Dresden-Rossendorf, Forschungsstelle Leipzig, Permoserstraße 15, 04318 Leipzig, Germany

Corresponding Author

*liyafei@njnu.edu.cn
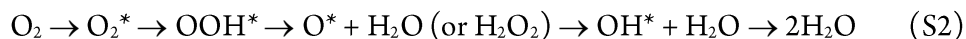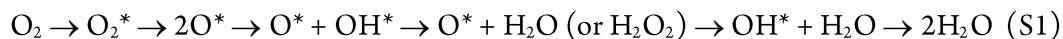
*thomas.heine@tu-dresden.de

Methods

Computational details.

Density functional theory calculations were carried out using projector-augmented wave approach[1,2] and the Perdew–Burke–Ernzerhof exchange-correlation functional,[3] as implemented in the VASP.[4,5] The cutoff energy was chosen at 500 eV, and the Brillouin zone was sampled using k-points of 0.02 Å^{-1}. Fermi-level smearing of 0.05 and 0.01 eV were adopted for PtTe and gas-phase species calculations, respectively. The convergence thresholds for energy and atomic forces were set as 1×10^{-5} eV and 0.01 eV/Å, respectively. The distance of vacuum space was set to about 20 Å. For multilayer systems, van der Walls interactions were included utilizing Grimme's D3 method.[6]

The phonon spectrum was computed using Phonopy code[7] with density functional perturbation theory (DFPT).[8] Molecular dynamic simulations were performed using the (4×4) PtTe supercell and the NVT ensemble, and were lasted for 10 ps with a time step of 1.0 fs, which was controlled by Nosé-Hoover method.[9] The climbing-image nudged elastic band (CI-NEB) method[10] as implemented in VASP was employed to simulate the reaction energy barrier.

ORR Mechanism.

The dissociative and associative mechanism pathways are generally the following equations (S1) and (S2), respectively.

$$O_2 \rightarrow O_2{}^* \rightarrow 2O^* \rightarrow O^* + OH^* \rightarrow O^* + H_2O \text{ (or } H_2O_2) \rightarrow OH^* + H_2O \rightarrow 2H_2O \text{ (S1)}$$

$$O_2 \rightarrow O_2{}^* \rightarrow OOH^* \rightarrow O^* + H_2O \text{ (or } H_2O_2) \rightarrow OH^* + H_2O \rightarrow 2H_2O \qquad \text{(S2)}$$

where * denotes an adsorption site. Note that the protons and electrons have been left out for clarity. The H_2O_2 is the product of the 2e ORR.

Reaction Free Energies.

We used a (3×3) supercell and explored the ORR performance of PtTe monolayer with the computational hydrogen electrode (CHE) model[11].

The free energy of each species (G) can be expressed as:

$$G = E_{DFT} + E_{ZPE} + \int C_p dT - TS \qquad \text{(S3)}$$

where E_{DFT}, E_{ZPE}, and S are ground state energy, zero point energy, and entropy, respectively. T is temperature taken as 298.15 K. For adsorbates, E_{ZPE} and S are obtained by vibrational frequencies calculations with harmonic approximation and neglecting contributions from the slab, while for molecules these are taken from the NIST database.[12] These contributions to free energies are listed in Table S1. Besides, solvent effects on OH* and OOH* have been considered by using the Poissson-Boltzmann implicit solavtion model[13]; the dielectric constant ε is taken as 80 for water. The free energy of O_2 was derived as $G_{O2} = 2G_{H2O} - 2G_{H2} - 4.92$ eV, since
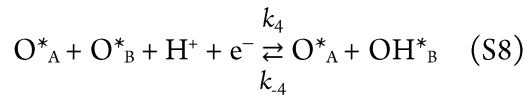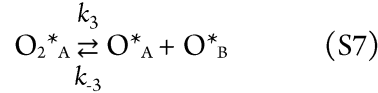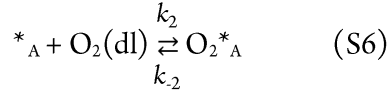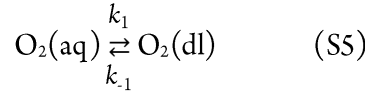
O_2 in triplet ground state is notoriously poorly described by DFT calculations. The adsorption free energy for the adsorbates (ΔG_{ads}), including O_2^* (ΔG_{O2^*}), O^*(ΔG_{O^*}), OH^* (ΔG_{OH^*}), and OOH^* (ΔG_{OOH^*}), can be calculated by:

$$\Delta G_{ads} = \Delta E_{ads} + \Delta E_{ZPE} - T\Delta S \quad (S4)$$

where ΔE_{ads} is adsorption energy of adsorbates, and ΔE_{ZPE} and ΔS are the difference of E_{ZPE}, and S, respectively.

Moreover, in accordance with the CHE model, the effects of electrode potential (U) and pH on ORR can be treated as an energy shift to free energy change in the electrochemical steps: $\Delta G_U = -eU$ and $\Delta G_{pH} = -k_BT\ln 10 \times pH$. The free energy diagram of ORR shown in this paper has performed a potential correction to be standard.

Polarization Curve Simulation.

Following the kinetic model developed by Hansen et al.,[14,15,16] we simulated the polarization curve of PtTe monolayer. Here, we focused on the dominating dissociative mechanism pathway, as O_2 dissociation on PtTe monolayer is identified to be quite thermodynamically and kinetically favourable. The O_2 molecule diffusion, adsorption, and electrochemical reduction steps are listed by the following equations:

$$O_2(aq) \underset{k_{-1}}{\overset{k_1}{\rightleftharpoons}} O_2(dl) \quad (S5)$$

$$*_A + O_2(dl) \underset{k_{-2}}{\overset{k_2}{\rightleftharpoons}} O_2{*}_A \quad (S6)$$

$$O_2{*}_A \underset{k_{-3}}{\overset{k_3}{\rightleftharpoons}} O{*}_A + O{*}_B \quad (S7)$$

$$O{*}_A + O{*}_B + H^+ + e^- \underset{k_{-4}}{\overset{k_4}{\rightleftharpoons}} O{*}_A + OH{*}_B \quad (S8)$$

$$O{*}_A + OH{*}_B + H^+ + e^- \underset{k_{-5}}{\overset{k_5}{\rightleftharpoons}} O{*}_A + *_B + H_2O \quad (S9)$$

$$O{*}_A + H^+ + e^- \underset{k_{-6}}{\overset{k_6}{\rightleftharpoons}} OH{*}_A \quad (S10)$$

$$OH{*}_A + H^+ + e^- \underset{k_{-7}}{\overset{k_7}{\rightleftharpoons}} *_A + H_2O \quad (S11)$$
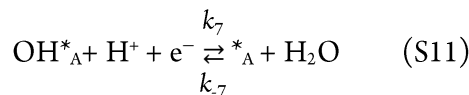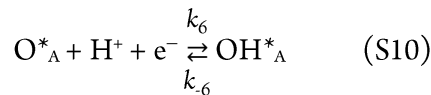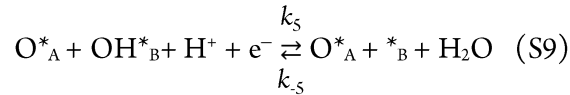
where the two different adsorption sites derived from O_2 dissociation are highlighted by $*_A$ and $*_B$. $O_2(aq)$ and $O_2(dl)$ represent O_2 in the electrolyte and the catalyst-electrolyte interface, respectively. Note that equations

(S5), (S6), and (S7) are non-electrochemical steps, and the rest of equations are electrochemical steps. Based on the above reduction steps, we can gained the rate equations of each species, such as,

$$\frac{\partial x_{O_2(dl)}}{\partial t} = k_1 x_{O_2(aq)} - k_{-1} x_{O_2(dl)} - k_2 x_{O_2(dl)} \theta_{*A} + k_{-2} \theta_{O_2*A} \quad (S12)$$

$$\frac{\partial \theta_{OH*A}}{\partial t} = k_6 \theta_{O*A} - k_{-6} \theta_{OH*A} - k_7 \theta_{O*A} + k_{-7} \theta_{*A} x_{H_2O} \quad (S13)$$

$$\frac{\partial \theta_{O*B}}{\partial t} = k_3 \theta_{O_2*A} \theta_{*B} - k_{-3} \theta_{O*A} \theta_{O*B} - k_4 \theta_{*B} + k_{-4} \theta_{OH*B} \quad (S14)$$

Here the $x_{O_2(aq)}$ and x_{H_2O} are taken as 2.34×10^{-5} and 1, respectively.[13] θ represents the coverage of the species.

These rate equations can be solved at steady state, and further infer the turn over frequency (TOF).

For non-electronchemical step i, its equilibrium constant (K_i) can be expressed as:

$$K_i = exp\left(-\frac{\Delta G_i}{k_B T}\right) \quad (S15)$$

where ΔG_i is the free energy change of step i, and k_B is the Boltzmann constant. The rate constant (k_i) is given by:

$$k_i = v_i \exp\left(-\frac{E_{a,i}}{k_B T}\right) \quad (S16)$$

where v_i is the pre-exponential factor, and $E_{a,i}$ is the activation energy.

While for electrochemical step, K_i is associated with the reaction potential (U vs. RHE), given by:

$$K_i = exp\left(-\frac{e(U - U_i)}{k_B T}\right) \quad (S17)$$

where U_i is the reversible potential of step i deduced by $U_i = -\Delta G_i/e$. And the k_i is written as:

$$k_i = A_i \exp\left(-\frac{E_{a,i}}{k_B T}\right) \exp\left(-\frac{e\beta_i(U - U_i)}{k_B T}\right) \quad (S18)$$

where A_i is an effective pre-exponential factor taken as 10^9, and β_i is the symmetric factor taken as 0.5.[15] Since the $E_{a,i}$ of electrochemical ORR steps are generally small, range from 0.10 to 0.26 eV,[17,18] we adopted $E_{a,i} = 0.25$ eV for all the electrochemical steps of ORR on PtTe monolayer.

Moreover, the rate constants for all the reverse reaction (k_{-i}), can be deduced by:

$$k_{-i} = \frac{k_i}{K_i} \quad (S19)$$

Finally, the current density (j) can be calculated by:

$$j = e\rho TOF_{e^-} \quad (S20)$$

Table S1. Zero-pint energy correction (E_{ZPE}), entropy contribution (TS), and total free energy correction ($G - E_{\mathrm{elec}}$) of the studied systems.

Species	E_{ZPE} (eV)	$-TS$ (eV)	$G - E_{\mathrm{elec}}$ (eV)
H_2	0.27	−0.40	−0.13
H_2O	0.56	−0.67	−0.11
O_2^*	0.13	−0.15	−0.02
O^*	0.07	−0.06	0.01
OH^*	0.34	−0.13	0.21
OOH^*	0.43	−0.21	0.22
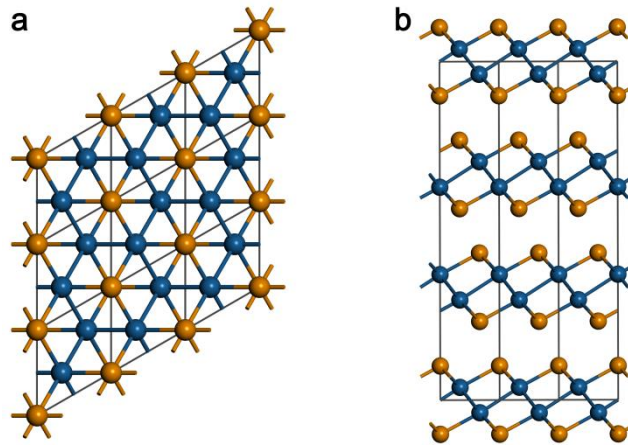
Figure S1. (a) Top and (b) side views of bulk PtTe. The blue and brown balls represent Pt and Te atoms, respectively.
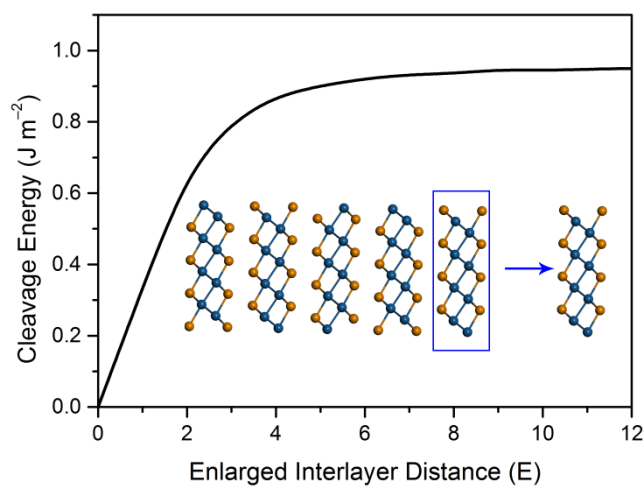
Figure S2. Cleavage energy estimation for the formation of PtTe monolayer. Increasing the distance between the exfoliated PtTe monolayer and bulk, the energy increases and reaches convergence at ~5 Å.
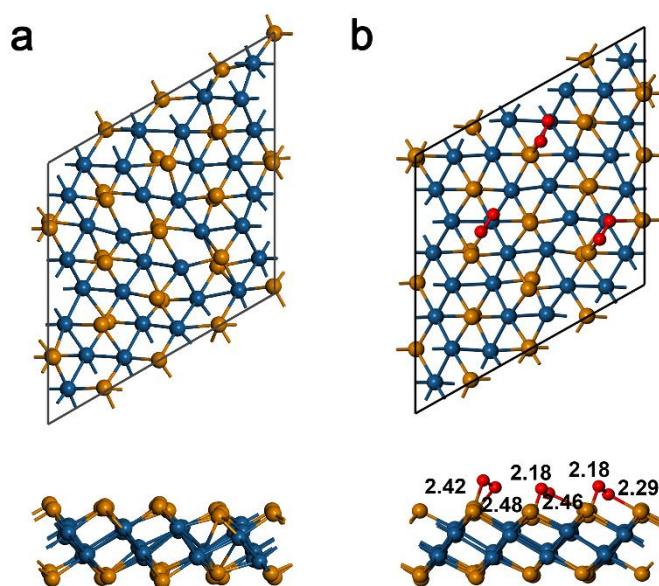
Figure S3. Snapshots of the equilibrium structure of (a) PtTe monolayer at 1200 K and (b) O_2 on PtTe monolayer at 300 K, respectively, at the end of 10 ps first-principles molecular dynamics simulation. The Te-O bond lengths are given in Å.
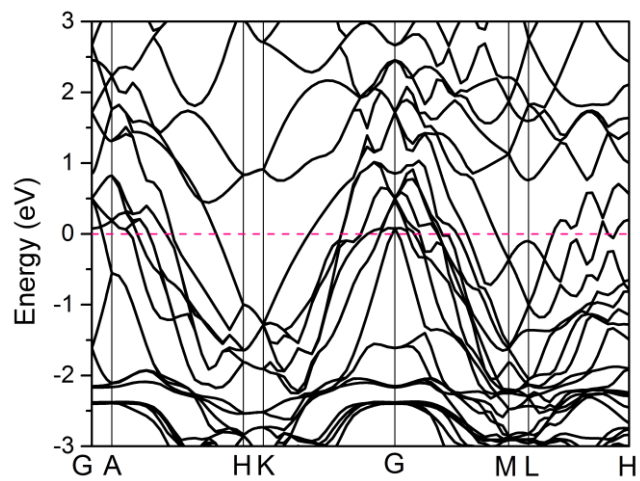
Figure S4. Band structure of bulk PtTe. The Fermi level is assigned at 0 eV.
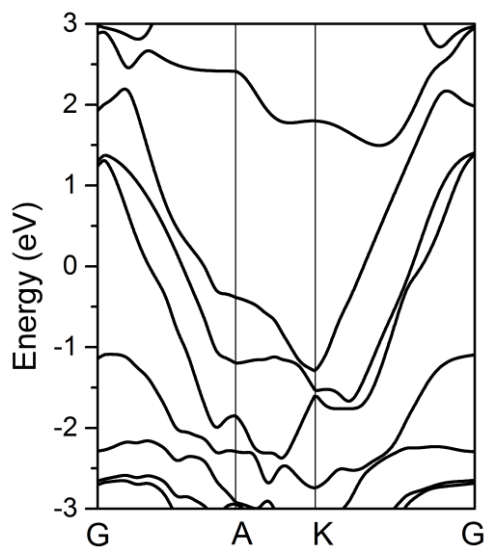
Figure S5. HSE06 band structure of PtTe monolayer. The Fermi level is assigned at 0 eV.
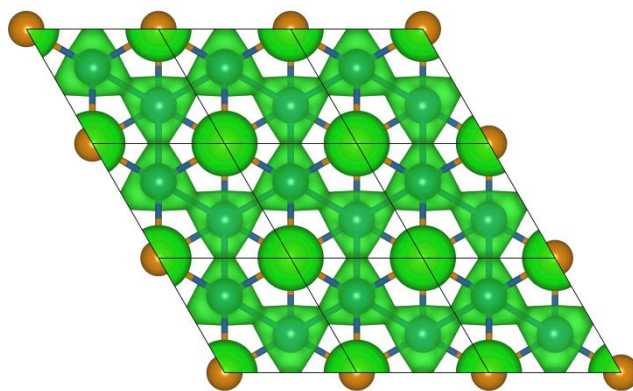
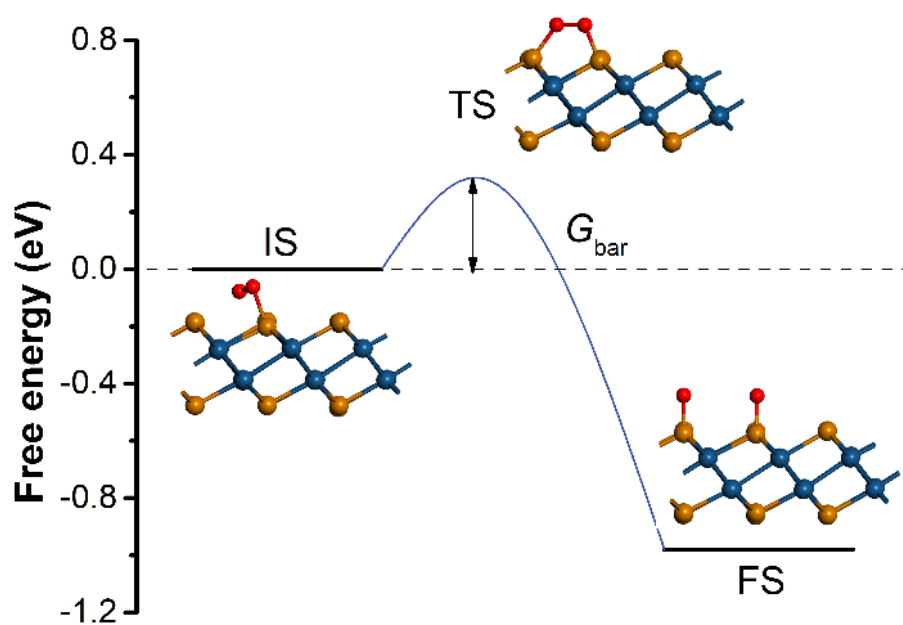**Figure S6.** Partial charge density around the Fermi level of PtTe Monolayer ($-0.5\ \text{eV} < E - E_{\text{F}} < 0\ \text{eV}$).

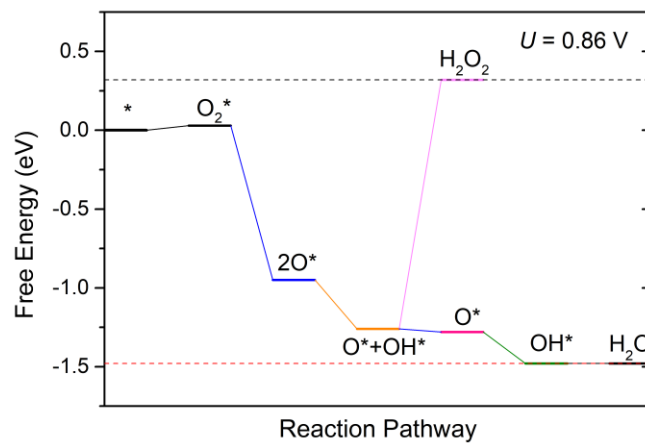**Figure S7.** O_2 dissociation on PtTe monolayer.

Figure S8. Free energy diagrams for the dissociative ORR pathway on PtTe basal plane at U = 0.86 V.
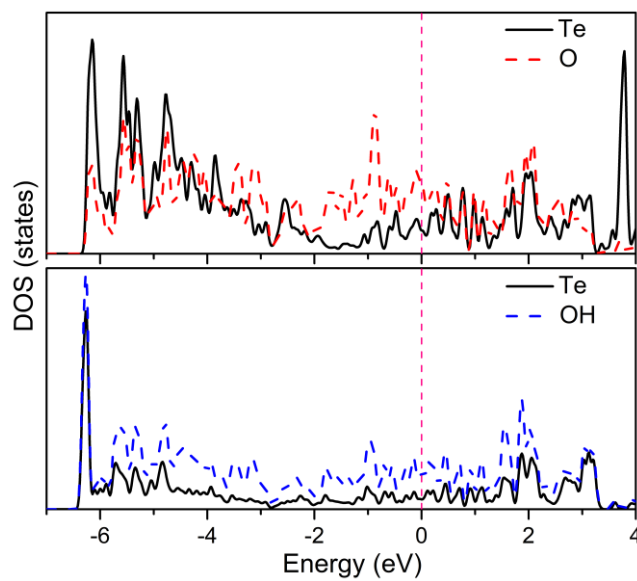

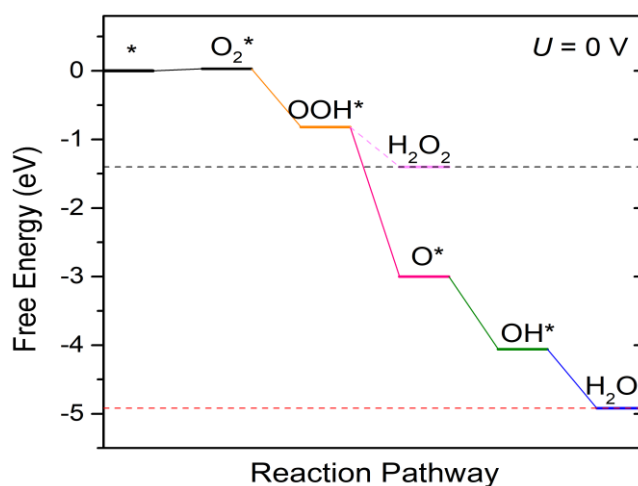**Figure S9.** Partial density of states of the intermediates and the Te site-5p orbital.

Figure S10. Free energy diagrams for the associative ORR pathway on PtTe basal plane at U = 0 V. The rate-determining step is the reduction of OH* to H_2O with a ΔG of −0.85 eV.
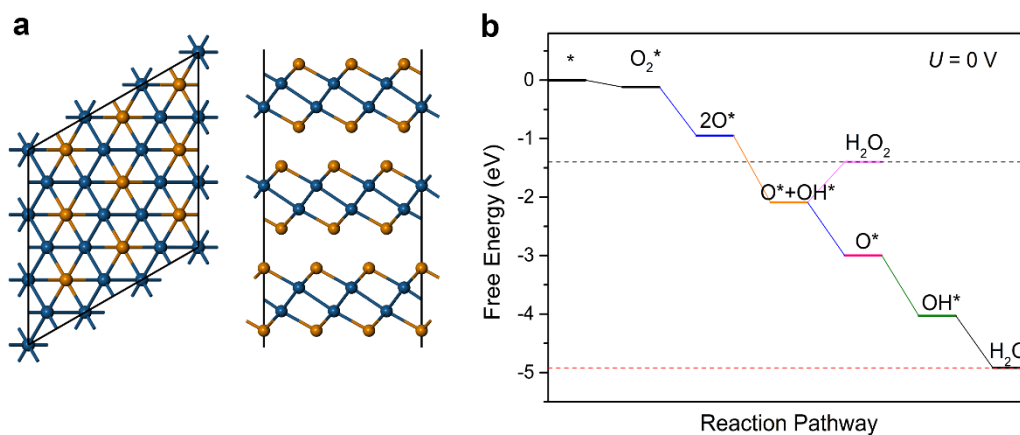

Figure S11. (a) Top (left) and side (right) views of PtTe trilayer in a 3×3 supercell. (b) Free energy diagram for ORR pathway on PtTe trilayer at U = 0 V. The rate-determining step is the reduction of OH* to H_2O with a ΔG of −0.89 eV.
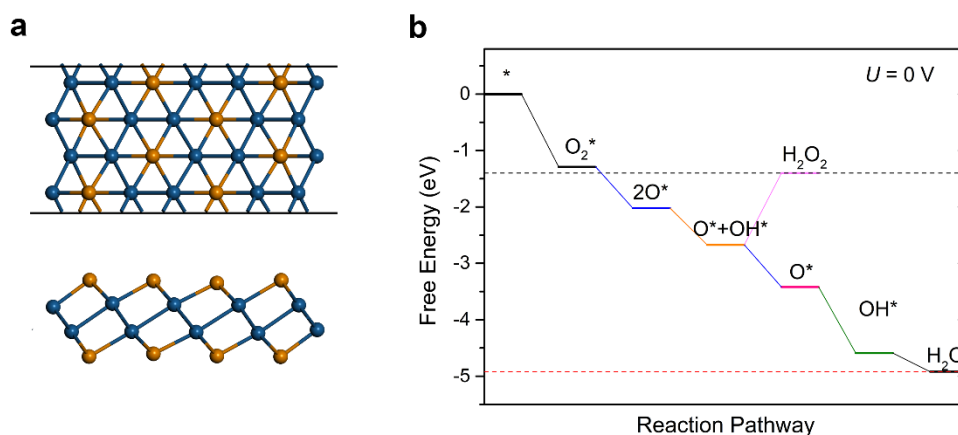
S10

Figure S12. (a) Top (upper) and side (bottom) views of edge sites of PtTe modeled by a ribbon model. (b) Free energy diagram for ORR pathway PtTe edge at U = 0 V. The rate-determining step is the reduction of OH*

to H_2O with a ΔG of just -0.33 eV due to the too strong binding strength of OH*.

References

[1] Blöchl, P. E. *Phys. Rev. B* **1994**, *50*, 17953.

[2] Kresse, G.; Joubert, D. *Phys. Rev. B* **1999**, *59*, 1758.

[3] Perdew, J. P.; Burke, K.; Ernzerhof, M. *Phys. Rev. Lett.* **1996**, *77*, 3865.

[4] Kresse, G.; Furthmüller, J. *Comput. Mater. Sci.* **1996**, *6*, 15.

[5] Kresse, G.; Furthmüller, J. Phys. Rev. B: Condens. Matter Mater. Phys. 1996, 54, 11169.

[6] Grimme, S.; Ehrlich, S.; Goerigk, L. *J. Comput. Chem.* **2011**, *32*, 1456.

[7] Togo, A.; Oba, F.; Tanaka, I. *Phys. Rev. B,* **2008**, *78*, 134106.

[8] Baroni, S.; De Gironcoli, S.; Dao Corso, A.; Giannozzi, P. *Rev. Mod. Phys.* **2001**, *73*, 515.

[9] Martyna, G. J.; Klein, M. L.; Tuckerman, M. E. *J. Chem. Phys.* **1992**, *97*, 2635.

[10] Henkelman, G.; Uberuaga, B. P.; Jonsson, H. *J. Chem. Phys.* **2000**, *113*, 9901.

[11] Nørskov, J. K.; Rossmeisl, J.; Logadottir, A.; Lindqvist, L.; Kitchin, J. R.; Bligaard, T.; Jónsson, H. *J. Phys. Chem. B* **2004**, *108*, 17886.

[12] Computational Chemistry Comparison and Benchmark Database. http://cccbdb.nist.gov/.

[13] Mathew, K.; Sundararaman, R.; Letchworth-Weaver, K.; Arias, T. A.; Hennig. R. G. *J. Chem. Phys.* 2014, **140**, 084106.

[14] Hansen, H. A.; Varley, J. B.; Peterson, A. A.; Nørskov, J. K. *J. Phys. Chem. Lett.* **2013**, *4*, 388

[15] Hansen, H. A.; Viswanathan, V.; Nørskov, J. K. *J. Phys. Chem. C* **2014**, *118*, 6706.

[16] Li, Y.; Zhang, S.; Yu, J.; Wang, Q.; Sun, Q.; Jena, P. *Nano Res.* **2015**, *8*, 2901.

[17] Tripković, V.; Skúlason, E.; Siahrostami, S.; Nørskov, J. K.; Rossmeisl, J. *Electrochim. Acta* **2010**, *55*, 7975.

[18] Wang, Y.; Yuan, H.; Li, Y.; Z. Chen, *Nanoscale,* **2015**, *7*, 11633.